

A Zero Thickness Cohesive Element Approach for Dynamic Crack Propagation using LS-DYNA[®]

Ala Tabiei* and Wenlong Zhang*

*Department of Mechanical and Materials Engineering, University of Cincinnati, Cincinnati, Ohio 45221, USA

Abstract

The zero thickness cohesive element approach for arbitrary crack propagation has a deficiency of introducing artificial compliance to the model, especially when cohesive elements are inserted into every element interfaces. For dynamic problems, the artificial compliance decreases the stress wave speed and makes the result less accurate. In this paper, the reason of the artificial compliance is examined, and the bilinear and exponential cohesive law are compared. The work shows that by choosing the right cohesive stiffness, element size and using bilinear cohesive law rather than exponential cohesive law, the artificial compliance issue can be limited to a negligible level without greatly increasing the computational time. Two numerical simulations are used to support the argument. According to our finding, in order to limit the artificial compliance and computational time, large element size is recommended. However, in fracture problems, small element size around crack tip is essential to capture the cohesive zone behavior. To escape the dilemma, we modify the cohesive zone enlargement approach presented in the literature [1] and adopt it for arbitrary crack propagation. The modified methodology enlarges the cohesive zone size by reducing the cohesive strength only around crack tips to allow more cohesive elements inside the cohesive zone. Two benchmark numerical simulations are carried out to verify the modified methodology.

1. Introduction

The concept of cohesive zone model was proposed by Dugdale (1960) [1] and Barenblatt (1962) [2]. The idea is to treat the process zone as a cohesive zone where there exists traction between two virtual surfaces ahead of the crack tip, whose behavior is governed by a traction-separation law, as shown in Figure 1.

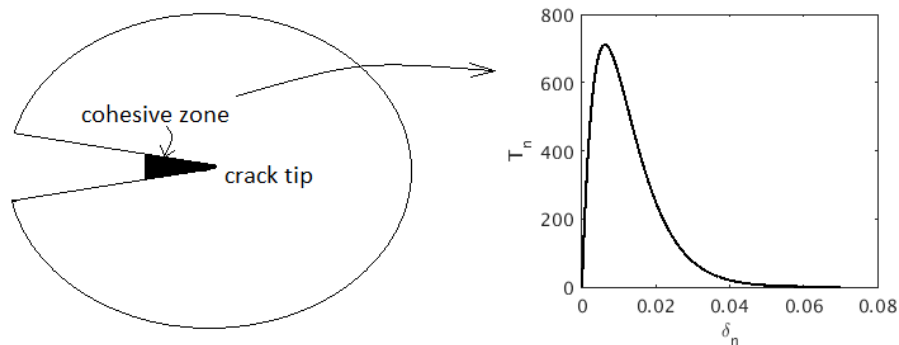


Figure 1. Cohesive zone at crack tip and cohesive law

Since cohesive zone model was proposed, it has been widely used in fracture problems especially crack propagation problems. It shows a much easier way to simulate crack propagation as no complicated failure criteria and topologies, but only the information of cohesive zone model is needed. It is very convenient and straightforward when the crack path is known ahead, so cohesive elements are only needed in that region, like composite delamination problems [3-5], crack propagation in beam bending problems [6,7] and fracture/fatigue in adhesive joints [8]. Zero thickness cohesive elements can also be inserted into every element interface to

allow arbitrary crack propagation. In 1994 Xu and Needleman [9] first used this approach to predict dynamic crack propagation.

At the same time, there are issues pertinent with the zero-thickness cohesive element approach. Researchers [10-13] have pointed out this zero-thickness cohesive element approach introduces artificial compliance to the model and could greatly alter the dynamic response when cohesive elements are applied at every element interface. There are several methods available to get rid of that extra compliance. The most straightforward one is to increase the initial stiffness of the cohesive model. That, however, is criticized for resulting in a big increase in computational time as time step is controlled by the elastic modulus of material [14]. Besides increasing the cohesive zone stiffness, an alternative approach was proposed by Camacho (1996) [14]. He used an initially rigid cohesive model and combined it with an element insertion topology to only add zero thickness cohesive elements at regions where a certain failure criterion is met. However, the insertion of cohesive elements requires complex topology and data structure for parallel computing and becomes unattractive for large-scale 3D problems [15]. Another way is to use hybrid discontinuous Galerkin/cohesive zone model method, in which discontinuous Galerkin formulation is used to eliminate jumps between element boundaries before failure [16,17].

Apart from initial stiffness in cohesive element, element size is also a factor that influences the artificial compliance. Klein (2001) used a 1-D model to illustrate that the artificial compliance is inversely proportional to the element size [11]. Furthermore, Blal (2012) [18,19] used a micro-mechanical model and homogenization technique to derive a function relating initial stiffness and element size to artificial compliance in 3D problems. His conclusion also suggests element size is inversely proportional to artificial compliance. Therefore, theoretically, we can choose big element sizes to limit the reduction of stiffness issue. Nevertheless, Tomar (2004) [20] pointed out there should be an upper bound for cohesive element size as well to guarantee enough number of cohesive elements inside the cohesive zone. This criterion is commonly adopted in the literature [10,21].

Turon (2006) [22] used a cohesive zone enlargement approach to increase the cohesive zone length by scaling down the cohesive strength, thus allowing big element sizes to be used. This methodology was proved to work well in delamination problem: the force-displacement results match well with small mesh cases, despite a small drop in the peak force, and that decrease is acceptable compared to the computational efficiency it brought. Harper (2008) [21] did study on both mode I and mode II delamination, and found increasing the cohesive zone length by reducing the cohesive strength will make the force-displacement curve smoother. Although it will produce a loss of stiffness in the elastic loading regime, it is relatively small magnitude if the reduce of cohesive strength is within a reasonable range. Z Shabir (2011) [23] tested the cohesive zone enlargement approach at intergranular level using Generalized Finite Element Method (GFEM). He found reducing the cohesive strength does not influence the crack path and force displacement curve. To the best of our knowledge, this method hasn't been used on arbitrary crack propagation problems, and that will be studied in this paper.

In this paper, the focus is on initially un-rigid cohesive element approach. It can be easily implemented into existing commercial FE code and doesn't need extra mesh topology and changes in shape function. We argue that by using the bilinear cohesive law, carefully choosing the initial stiffness, and guaranteeing no extra mass is introduced, the artificial compliance and wave speed change can be limited within a negligible range and the increase of the simulation time is also affordable. Moreover, cohesive zone enlargement approach is adopted in arbitrary crack propagation to allow the use of relatively coarse mesh.

The paper is structured in the following way: in Section 2, a study of the relationship between cohesive stiffness, element size and artificial compliance is carried out; two numerical simulations are presented to demonstrate that if choosing the cohesive stiffness and element size to be in the right range, the artificial compliance and the change of dynamic wave speed is negligible. Based on the result of Section 2, a comparison of the bilinear law and exponential law is given in Section 3 in terms of their initial stiffness. To make coarse element usable in arbitrary crack propagation problem, we modified the cohesive zone enlargement approach and programmed it into LS-DYNA's user subroutine in Section 4. Two benchmark studies are presented in Section 5 to verify the modified cohesive zone enlargement approach.

2. Zero thickness cohesive elements and wave speed

Regarding the artificial compliance issue with zero-thickness cohesive elements, it seems the only way to compensate it in the framework of cohesive element approach is to use high elastic modulus in the cohesive element. In 2001, Klein [11] used a 1D example (Figure 2) to illustrate the relationship between cohesive element stiffness and effective elastic modulus:

$$E_{\text{eff}} = E \left[1 - \frac{1}{1 + (Kh/E)} \right] \tag{1}$$

where h is solid element length, K is the stiffness of cohesive element, E is the elastic modulus of solid element and E_{eff} is the effective modulus of the whole model.

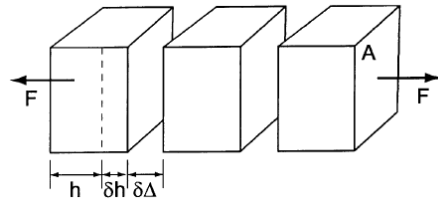


Figure 2. Illustration of artificial compliance in 1D [24]

From Equation (1), it can be observed that increasing the cohesive stiffness and element size would make effective modulus closer to solid element elastic modulus. In 2013, Blal [19] used a micromechanical model and a homogenization technique to estimate the relationship between cohesive stiffness, element size and effective elastic modulus (Equation (2~3)):

$$\frac{E_{\text{eff}}}{E} = \frac{\xi}{1 + \xi} \text{ where } \xi = \frac{5}{1 + (4/3)(K_n/K_t)} \times \frac{K_n}{EZ} \tag{2}$$

$$\frac{v_{\text{eff}}}{v} = \frac{15K_n v + (2 K_n/K_t - 1)EZ}{1515K_n v + (4 K_n/K_t + 3)EZ} \tag{3}$$

where A is the total element surface area, V is the total volume of the meshed body, Z is a value based on mesh type, and K_n, K_t are the initial normal and tangential stiffness in cohesive law respectively. Taking $Z = 6$ for structured tet mesh, as suggested in [19], we can plot K_n/E vs. E_{eff}/E curve (Figure 3). It can be observed from Figure 3 that to make the overall elastic modulus 95% of the original elastic modulus, the cohesive stiffness needs to be about 30 times of the elastic modulus. To meet that requirement bilinear cohesive law instead of exponential cohesive law should be used, and the reason will be explained in Section 3. In dynamic problem, attention has to be paid not only to initial stiffness, but also to the mass of cohesive elements. It must be guaranteed that no extra mass is introduced by cohesive elements.

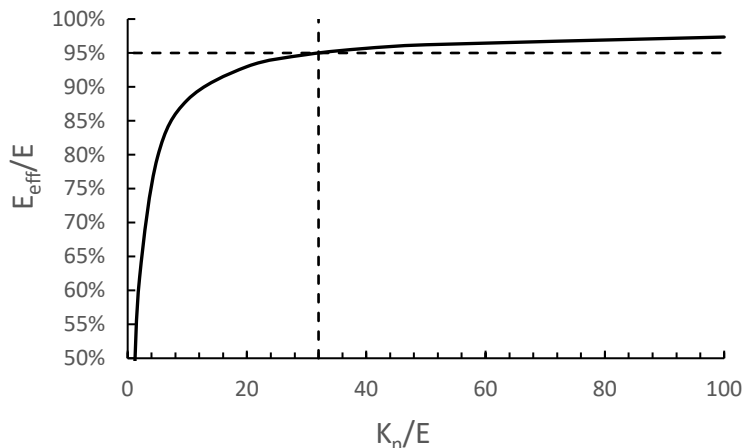


Figure 3. Cohesive stiffness vs. effective elastic modulus using Blal’s micromechanics model [19]

2.1. Influence of cohesive elements on the compressive stress wave speed in a 3D bar model

To test the theory in 3D cases, we simulated wave propagation in a steel bar using commercial FE code LS-DYNA. The dimension of the steel bar is shown in Figure 4. The bar is loaded at one end by a step load and fixed at the other end. The stress wave at the fixed end is obtained, and wave speed is calculated. A bilinear cohesive law is used so that arbitrary initial stiffness can be chosen. The amplitude of the step load is small enough, so the traction and separation remain in the ascending part of cohesive law during the whole process. The effective elastic modulus of the bar with cohesive elements is also obtained by a quasi-static loading. Figure 5(a) shows the relationship between effective elastic modulus and cohesive stiffness, with element size equals 2mm. Figure 5(b) shows the relationship between effective elastic modulus and element size in longitudinal direction and $K_n/E = 10$. This agrees with the results in 1D model.

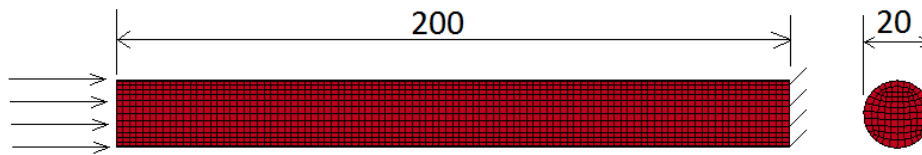


Figure 4. A 3D steel bar model under a step load

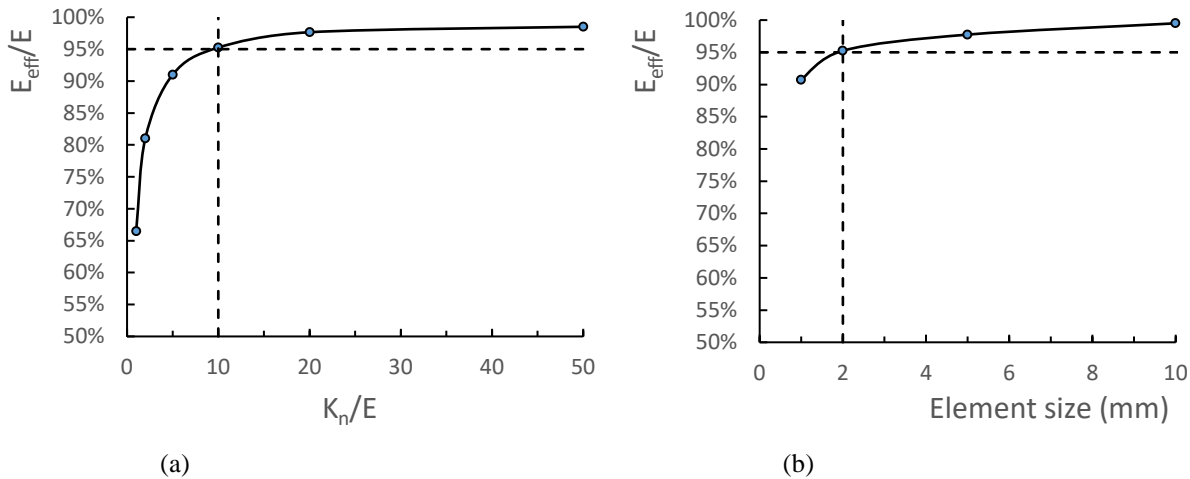


Figure 5. (a) Cohesive stiffness vs E_{eff} , (b) Element size vs. E_{eff}

In wave propagation simulation, 2mm mesh size is used. The stress wave history of case $K_n/E = 20$ is compared to a case without cohesive element (Figure 6). For a 2mm mesh size, $K_n/E = 20$ would give an effective elastic modulus 98% of solid the elastic modulus. $K_n/E = 10$ and $K_n/E = 50$ are also used for comparison (Figure 7). The wave speed for each case is also computed and summarized in Table 1. It can be observed from Figure 6~7 and Table 1 that for $K_n/E = 20$ the compressive stress wave speed is around 2% of error. For $K_n/E = 50$, there is a 85.3% of reduction in time step, which corresponds to a 5.5 times of increase in the computing time.

Table 1. Wave speed and time step reduction for different cohesive stiffness when mesh size is 2mm

	No cohesive	$K_n/E = 10$	$K_n/E = 20$	$K_n/E = 50$
Wave speed (m/s)	5167	5000	5153	5164
Error (%)	--	3.18	2.07	0.23
Time step (dt)	1.13e-4	3.71e-5	2.62e-5	1.66e-5
dt reduction (%)	--	67.2	76.8	85.3

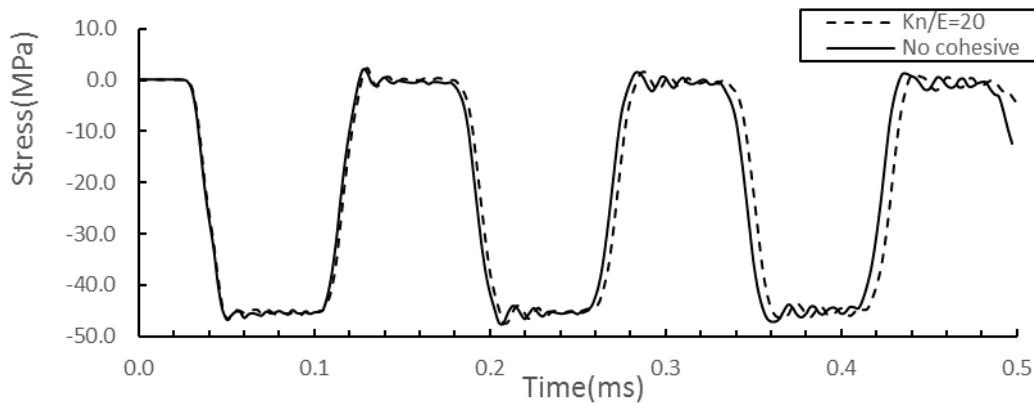


Figure 6. Compressive stress wave history at the fixed end of the 3D bar

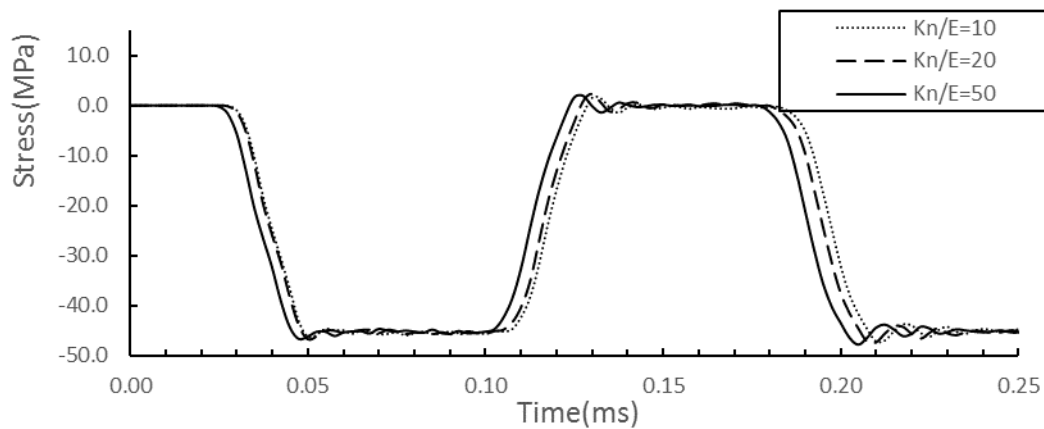


Figure 7. Compressive stress wave history at the fixed end of the 3D bar for different cohesive stiffness

2.2. Influence of cohesive elements on the shear stress wave speed in a 3D plate model

This simulation will investigate the shear wave speed in a plane with cohesive elements at every element interface. In this simulation, a plate with size $100\text{mm} \times 100\text{mm} \times 1\text{mm}$ is modelled using solid elements (Figure 8). The plate is fixed at three edges and loaded at the free edge under a constant force loaded at a width of 4mm . The plate is modelled with 1mm mesh size. Aluminum 2024 T3 is used; it has an elastic modulus $E = 72\text{GPa}$, shear modulus $G = 28\text{MPa}$, Poisson's ratio $\nu = 0.3$ and density $\rho = 0.27\text{g/cm}^3$. The shear stress history at a point $25\text{mm} \times 25\text{mm}$ from the left down corner is extracted and plotted for different cohesive zone initial stiffness. The same cohesive initial stiffness is used for both normal and tangential direction. The shear stress history is plotted in Figure 9~10 and the time step reduction is summarized in Table

2. The wave speed reduction is negligible (0.4%) when $K_n/E = 50$, and the time step is reduced 85%, which corresponds to a 5.5 times of increase in the simulation time.

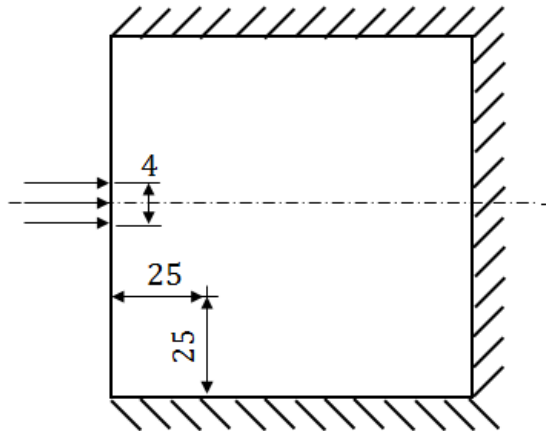


Figure 8. Illustration of the plate model (units: mm)

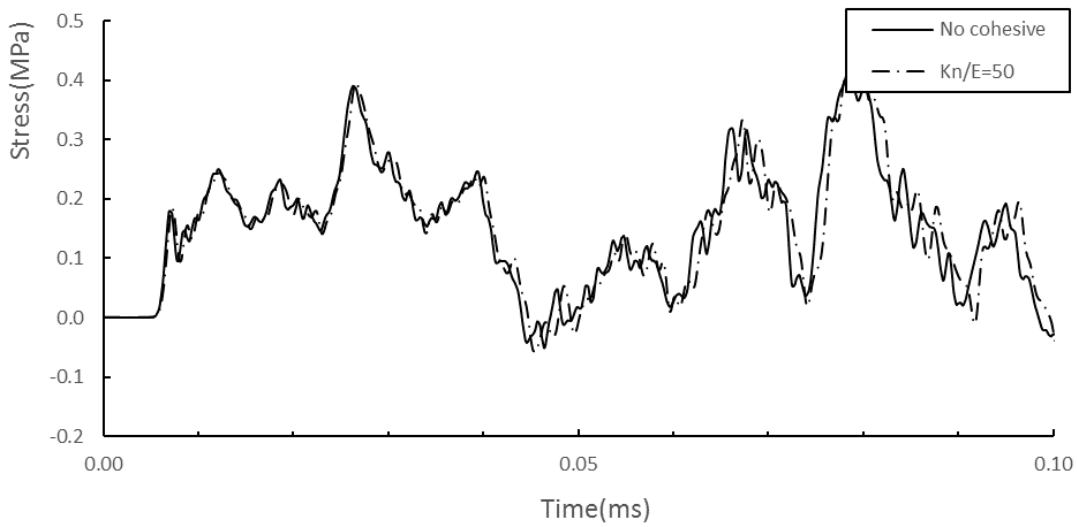


Figure 9. Shear Stress wave history at a fixed point on the plate

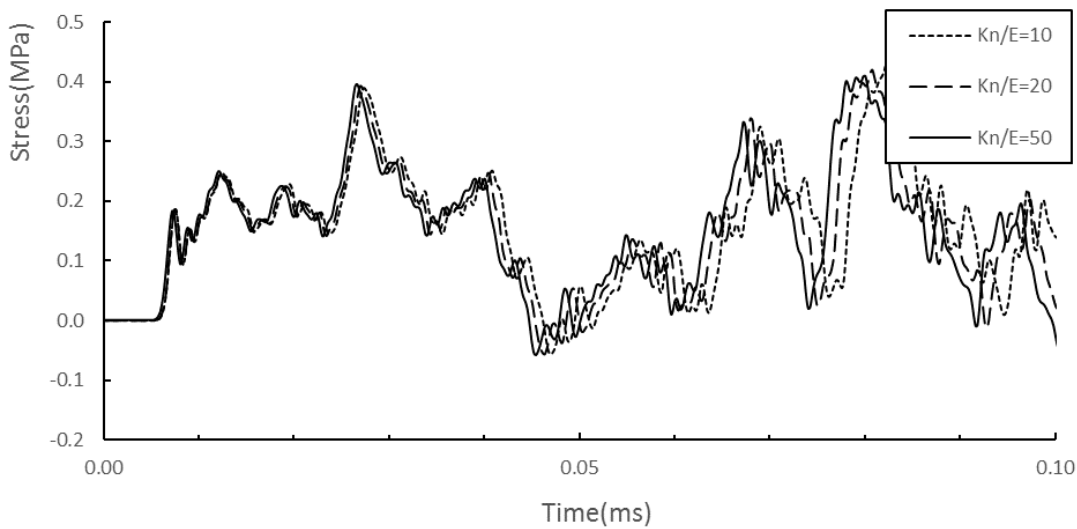


Figure 10. Shear Stress wave history at a fixed point on the plate for different cohesive initial stiffness

Table 2. Shear wave speed and time step reduction for different cohesive stiffness

	No cohesive	$K_n/E = 10$	$K_n/E = 20$	$K_n/E = 50$
Wave speed (m/s)	6799	6347	6559	6772
Error (%)	--	6.65	3.53	0.39
Time step (dt)	1.13e-4	3.71e-5	2.74e-5	1.73e-5
dt reduction (%)	--	67.2	75.8	84.7

Based on the above two simulations, we can prove that by properly choosing the cohesive stiffness and element size, the artificial compliance can be limited within negligible range. Also, there are some observations that can serve as a guideline for future modeling:

- 1) Avoid using extremely small element size.
- 2) The cohesive initial stiffness does not need to be extremely high because once it reaches a certain value (98% in this case), a further increase in cohesive stiffness would only reducing the time step without increasing effective elastic modulus much.

3. Bilinear cohesive vs. exponential cohesive law on their initial stiffness

Based on the result of Section 2, the initial stiffness of cohesive element needs to be in the right range to reduce the artificial compliance to a negligible range, and that requires the cohesive law to have a high slope in the ascending part. In this section, we argue that unlike bilinear cohesive law, exponential cohesive fails to meet this requirement for many materials. Many authors who pointed out huge artificial compliance were using exponential cohesive law [10,25-27].

The initial stiffness of bilinear cohesive law is quite straightforward; it can be taken any value as long as the separation condition is satisfied: the corresponding separation at maximum traction should be smaller than the largest separation in the cohesive model, which is determined by Equation (4):

$$\delta_n = \frac{2G_{IC}}{T}, \delta_t = \frac{2G_{IIC}}{S} \quad (4)$$

where δ_n and δ_t are the maximum separation in normal and tangential direction; G_{IC} and G_{IIC} are the critical energy release rate in mode I and mode II respectively and T, S corresponds to the cohesive strength in normal and shear direction.

For the exponential law, we use the modified Xu-Needleman's cohesive law [28] as an example. The traction in normal and tangential directions are shown as follows:

$$T_n = \frac{G_{IC}}{\delta_n} \left(\frac{\Delta_n}{\delta_n} \right) \exp \left(-\frac{\Delta_n}{\delta_n} \right) \exp \left(-\frac{\Delta_t^2}{\delta_t^2} \right) \quad (5)$$

$$T_t = 2 \frac{G_{IIC}}{\delta_t} \left(\frac{\Delta_t}{\delta_t} \right) \left(1 + \frac{\Delta_n}{\delta_n} \right) \exp \left(-\frac{\Delta_n}{\delta_n} \right) \exp \left(-\frac{\Delta_t^2}{\delta_t^2} \right) \quad (6)$$

where $\delta_n = G_{IC}/(eT)$, and $\delta_t = G_{IIC}/(S\sqrt{e/2})$. The initial stiffness in normal and tangential direction are $K_n = G_{IC}/\delta_n^2$ and $K_t = 2 G_{IIC}/\delta_t^2$ respectively. Replacing δ_n and δ_t by expressions of normal and tangential strength, the initial stiffness can be rewritten as:

$$K_n = \frac{e^2 T^2}{G_{IC}}, K_t = \frac{e S^2}{G_{IIC}} \quad (7)$$

Thus the initial stiffness is determined by critical energy release rate and cohesive strength, so it is a constant value that only relates to material properties. This value varies for different materials and for many materials it is not much higher, or even lower, than the elastic modulus. To illustrate how exponential cohesive law can

introduce artificial compliance, the initial stiffness of several materials are calculated and summarized in Table 3.

Table 3. Initial stiffness in exponential cohesive law for different materials

Material	G_{IC} (MPa · mm)	f_t (MPa)	K_n (GPa)	E (Gpa)	K_n/E
Concrete [29]	0.08	3	0.831	31.4	0.0265
PMMA [30]	0.5	48	34.0	1.80	18.9
Steel AISI 4340 [31]	12.5	745	328	200	1.64
Aluminum 2024 T3 [32]	8.55	483	202	73.1	2.76

For the four materials listed above, none of them has an initial cohesive stiffness higher than 20 times of elastic modulus, which is the value that corresponds to $E_{\text{eff}} = 98\%E$ in our 3D steel bar model. For concrete, the initial stiffness in exponential cohesive law is even smaller than its elastic modulus. As a result, exponential cohesive law would introduce large artificial compliance if zero thickness cohesive elements are used between every element. However, in cases where only one or a few layers of cohesive elements are used, and exponential cohesive law can still be used.

4. Cohesive zone enlargement approach

Tomar (2007) [33] pointed out that it is necessary to keep the cohesive element small enough, so there are enough elements inside the cohesive zone to capture its behavior. The cohesive zone length is a function of elastic modulus, maximum traction, and surface energy, and it has been estimated by many authors [34,35]. Take Rice's estimation as an example [35]:

$$l_c = \frac{9\pi EG_{IC}}{32 \sigma_t^2} \quad (8)$$

The minimum number of cohesive elements that should be in the cohesive zone is not a universally agreed issue in the literature. Falk (2004) [10] suggested more than five cohesive elements inside the cohesive zone to capture the crack tip behavior. Harper (2008) [21] suggested more than three elements in delamination problems. Assuming three elements need to be in the cohesive zone, the corresponding element size for different materials are calculated and summarized in Table 4.

Table 4. Cohesive zone length for different materials

Material	G_{IC} (MPa · mm)	f_t (MPa)	E (Gpa)	l_c (mm)	Element size (mm)
Concrete [29]	0.08	3	31.4	246	82.1
PMMA [30]	0.5	48	1.80	0.345	0.115
Steel AISI 4340 [31]	12.5	745	200	3.98	1.33
Aluminum 2024 T3 [32]	8.55	483	73.1	2.37	0.789

As shown in Table 4, except for concrete, all other materials need very small cohesive element size required to capture the crack tip behavior, and using such small element size would not only increase the artificial compliance but also increase the computational cost.

Turon's cohesive zone length enlargement approach is adopted and modified in this paper so relieve the cohesive zone size restraint [33]. Its idea is to enlarge the cohesive zone length by decreasing the maximum traction in the cohesive model. In this way, larger mesh size is allowed, and the cohesive zone behavior can still be captured. Modified cohesive strength near crack tip can be obtained by equating the cohesive zone length to cohesive element length multiplies the number of elements inside the cohesive zone:

$$T = \sqrt{\frac{9\pi E G_{Ic}}{32l_c}} = \sqrt{\frac{9\pi E G_{Ic}}{32N_e l_e}} \quad (9)$$

where N_e is the number of cohesive elements inside the cohesive zone, and l_e is the cohesive element length. In Equation (9) the number of cohesive elements inside the cohesive zone is taken as an input.

A topology is developed that reduces the cohesive strength only near the crack tip, so that it can be applied to arbitrary crack propagation without changing the global behavior. For each time step, the newly failed cohesive elements are taken as a crack tip, and their coordinate information is stored. The distance from other cohesive elements to crack tip is calculated, and if it falls within a range, the cohesive strength of these elements would be decreased to enlarge the cohesive zone. This algorithm is programmed into the bilinear cohesive law in a user-defined material subroutine in LS-DYNA. Two benchmark studies are presented in next section to prove the feasibility of the modified cohesive zone enlargement approach.

5. Benchmark study

5.1. Benchmark study Kolthoff plate impact problem

Kolthoff plate impact problem has been used by many people for crack propagation verification [36,37]. A plate with two symmetric initial cracks is impacted by a projectile at initial speed of $V_0 = 20m/s$ to make the plate have brittle failure. Due to the symmetry of the plate and boundary condition, only half of the plate is modelled. A schematic illustration of the specimen is shown in Figure 11. The material property of the plate is $E = 190GPa$, $\nu = 0.3$ and $\rho = 8000kg/m^3$. $K_I = 68MPa\sqrt{m}$ is used in cohesive model [36]. Three mesh sizes (1mm, 2mm, and 3mm) are used to study how cohesive zone enlargement approach allows the use of relatively coarse mesh. Based on the study in Section 2, cohesive stiffness is taken as 50 times of the elastic modulus, which should keep the effective elastic modulus larger than 98% of E.

Figure 12~13 show the crack shape for all the mesh cases with and without cohesive zone enlargement approach. For cases with cohesive zone enlargement method, the number of elements in the cohesive zone is 6, 3 and 2 for mesh size 1mm, 2mm, and 3mm respectively. The cohesive strength near crack tip is reduced to increase the cohesive zone length. As a result, it helps improve the crack shape in the 3mm mesh size case, and the inclined angle from horizontal line is close to 70° obtained from experiment [36], as shown in Figure 14.

Crack propagation speed is calculated using Equation (10) and is plotted in Figure 15. The average crack propagation speed is around $2000m/s$, which agrees well with the result in [38]. Enlarging cohesive zone length does not have a distinguishable influence on the wave speed. The crack propagation history for 2mm mesh size case is plotted in Figure 16, and it agrees well with the results of Extended Finite Element Method (XFEM) and peridynamic result [30,37].

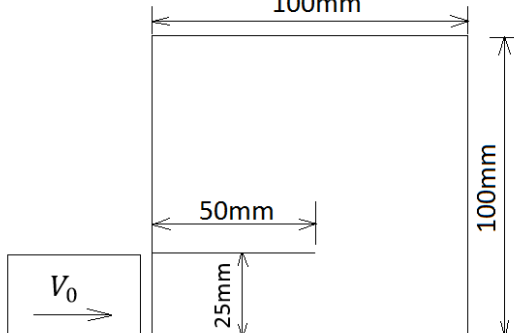
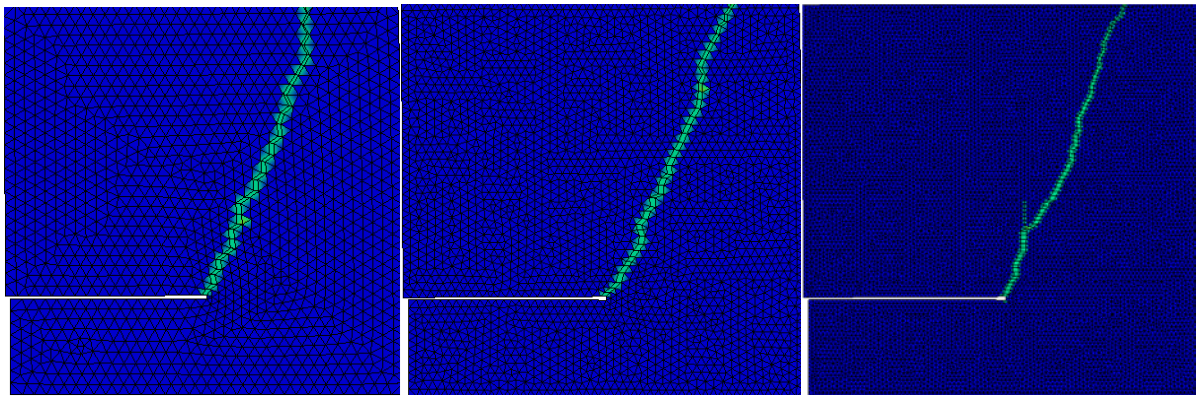
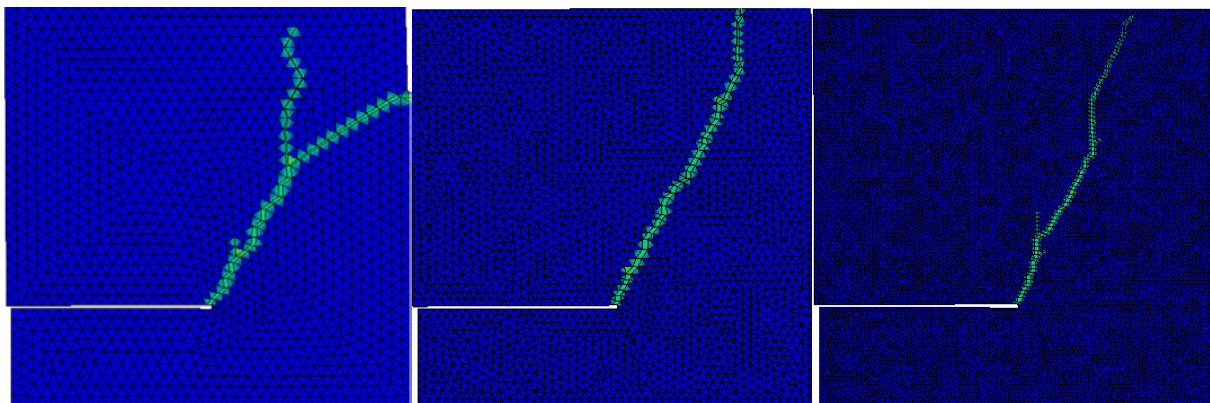
$$V = \frac{d_{i+1} - d_i}{t_{i+1} - t_i} \quad (10)$$


Figure 11. Illustration of Kalthoff experiment



(a) Mesh size 3mm (b) Mesh size 2mm (c) Mesh size 1mm

Figure 12 . Crack shape for all the mesh cases with cohesive zone enlargement approach



(a) Mesh size 3mm (b) Mesh size 2mm (c) Mesh size 1mm

Figure 13. Crack shape for all the mesh cases without cohesive zone enlargement approach

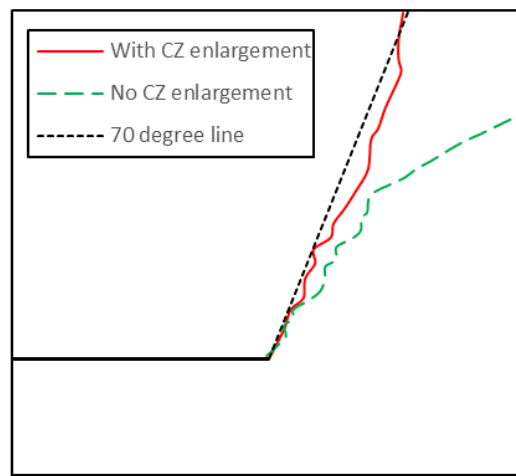


Figure 14. Comparison between crack shape of 3mm mesh case with and without cohesive zone enlargement method

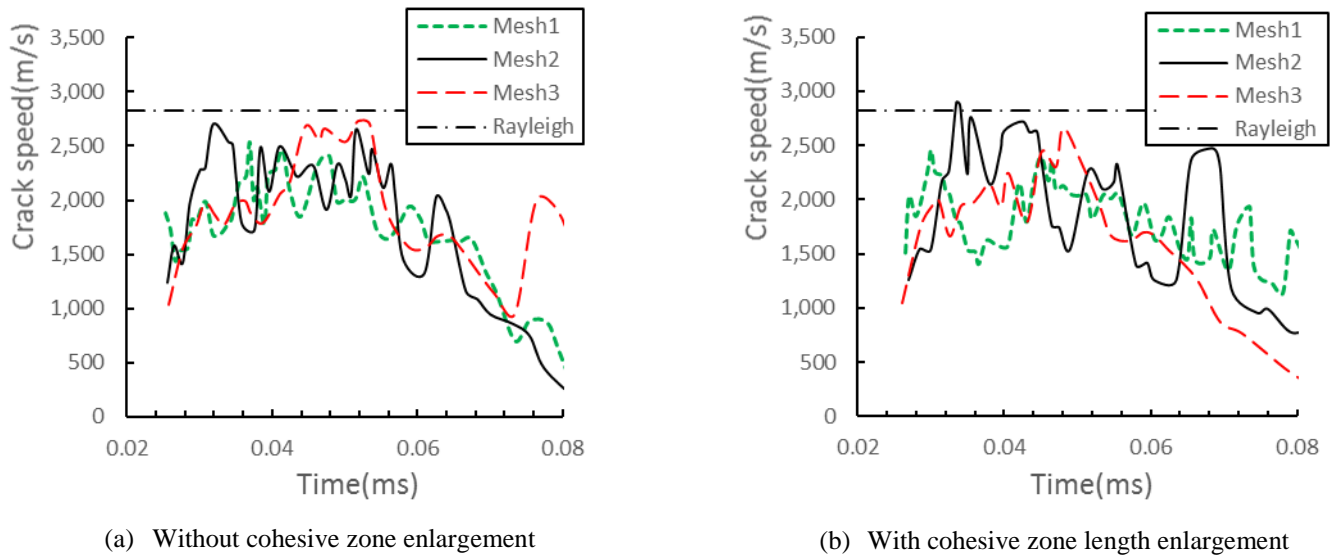


Figure 15. Wave speed for cases with and without cohesive zone length enlargement

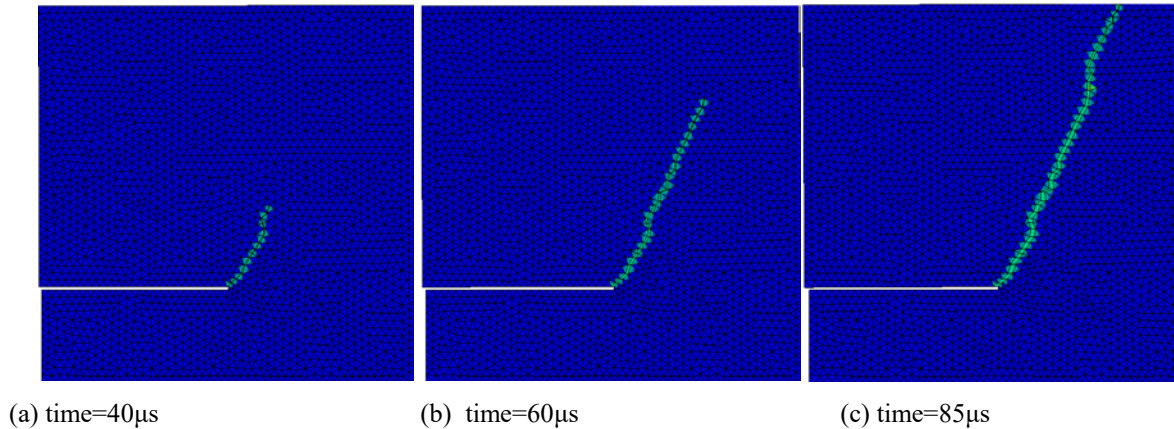


Figure 16. Crack propagation history for mesh size 2mm model with cohesive zone enlargement approach

5.2. Dynamic crack branching

This benchmark test involves dynamic crack branching in a pre-notched glass plate. This example has been applied in many papers [30,38,39] to verify the ability of a method to predict dynamic crack branching, such as Element Free Galerkin (EFG) method [38], XFEM [30] and peridynamics method [39]. We aim to use this simulation to show that the cohesive zone enlargement approach helps capture the crack branching shape with a coarse mesh.

The geometry and boundary condition of the specimen is shown in Figure 17. The material property used are $E = 32\text{GPa}$, $\nu = 0.2$, and $\rho = 2450\text{ kg/m}^3$. The critical energy release rate $G_{IC} = G_{IIC} = 0.003\text{ N/mm}$ is adopted from [30]. We use $\delta_{max} = 1.2 \times 10^{-3}\text{ mm}$ for the bilinear cohesive law. 3D 6-node solid element and 8-node cohesive element are used in the model and the mesh size is 1 mm for the whole model. According to Section 4, a typical cohesive zone length for glass is around 0.4 mm , thus for 1 mm mesh size, the predicted behavior is that it cannot capture the correct crack shape since there is not enough elements inside the cohesive zone. With cohesive zone enlargement approach, however, instead of using high density mesh to capture the high stress field around crack tip, the cohesive strength around crack tip is reduced to give the same effect. When cohesive zone enlargement approach is used, a minimum number of 3 cohesive elements is guaranteed within the cohesive zone by reducing the cohesive strength, and the critical energy release rate is reduced

correspondingly so that the maximum separation remains unchanged. Algorithm is implemented in user-defined cohesive material model in LS-DYNA to find elements around crack tips, and only these elements have reduced cohesive strength, thus avoiding altering the material property of the whole model.

The crack shape at different times are plotted in Figure 18 for cases with and without cohesive zone enlargement approach. As shown in Figure 18, using cohesive zone enlargement approach captures the dynamic crack branching very well, compared to the result using XFEM approach [30], as shown in Figure 19. To further verify the method, crack propagation speed is extracted and compared to the XFEM result [30], as shown in Figure 20. The Rayleigh speed is 2050m/s according to [38]. Similar to XFEM result [30], the crack propagation speed quickly increases to a maximum of 2000m/s around 0.003ms and crack branching occurs after that.

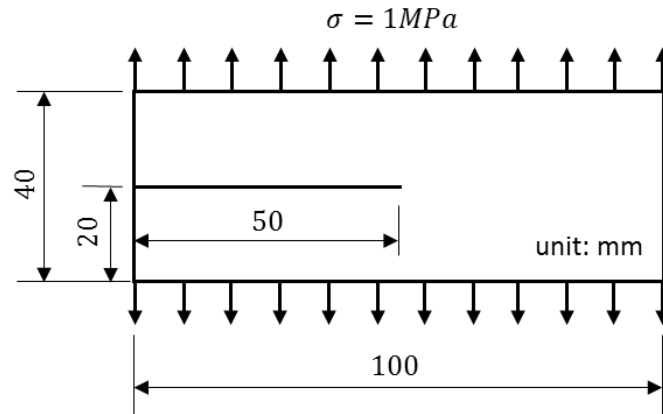


Figure 17. Geometry and boundary condition of the plate

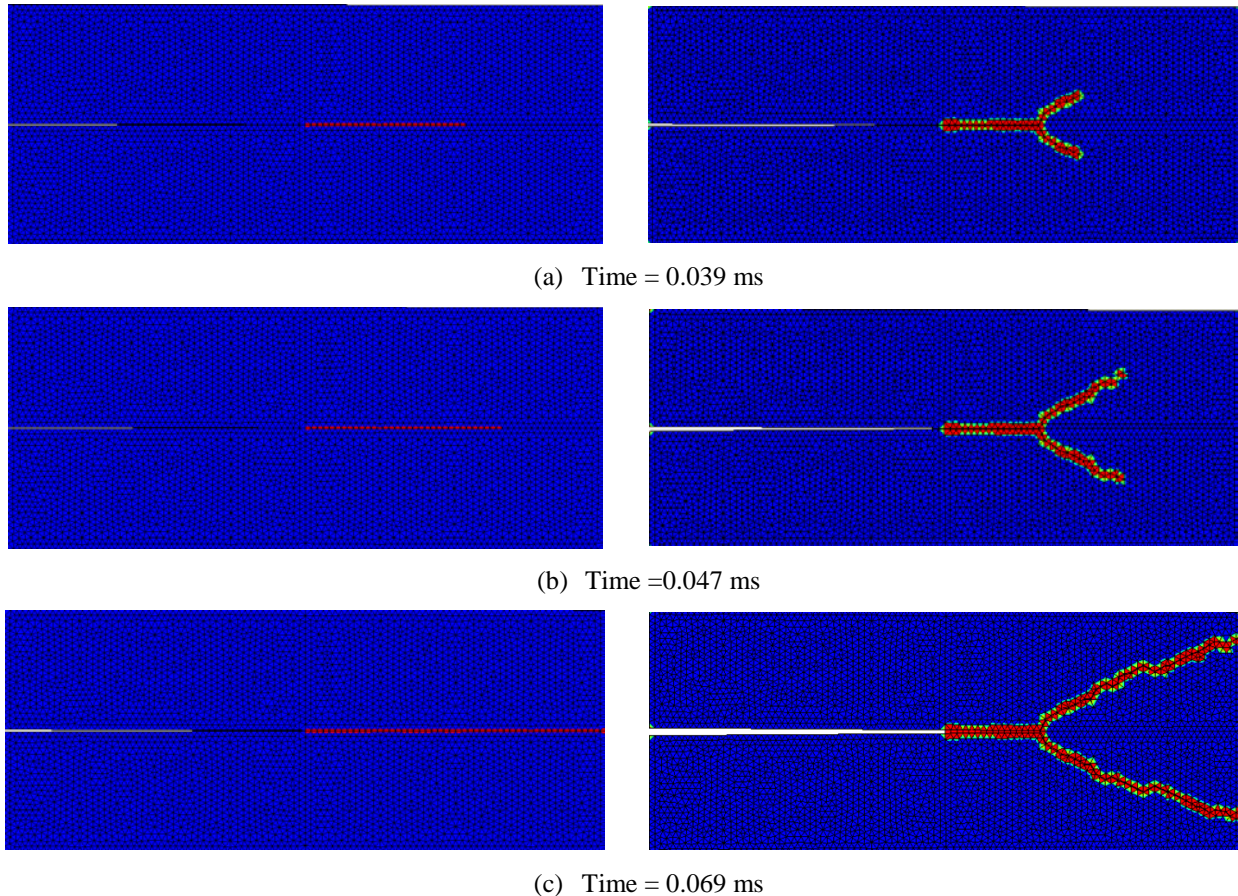
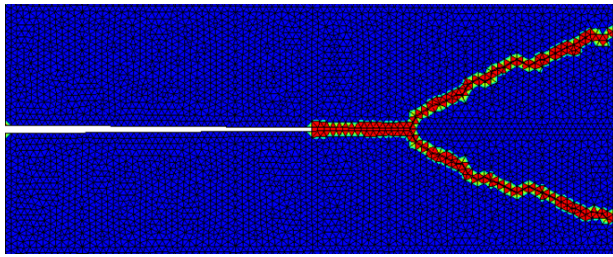
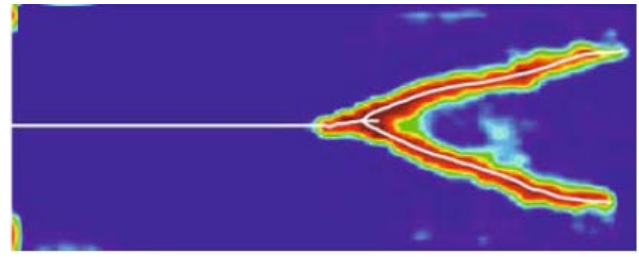


Figure 18. Crack propagation with time. Left column: crack shape without cohesive zone enlargement approach; Right column: crack shape with cohesive zone enlargement approach



(a) Cohesive element method



(b) XFEM [30]

Figure 19. Final crack path comparison between cohesive element method and XFEM from literature

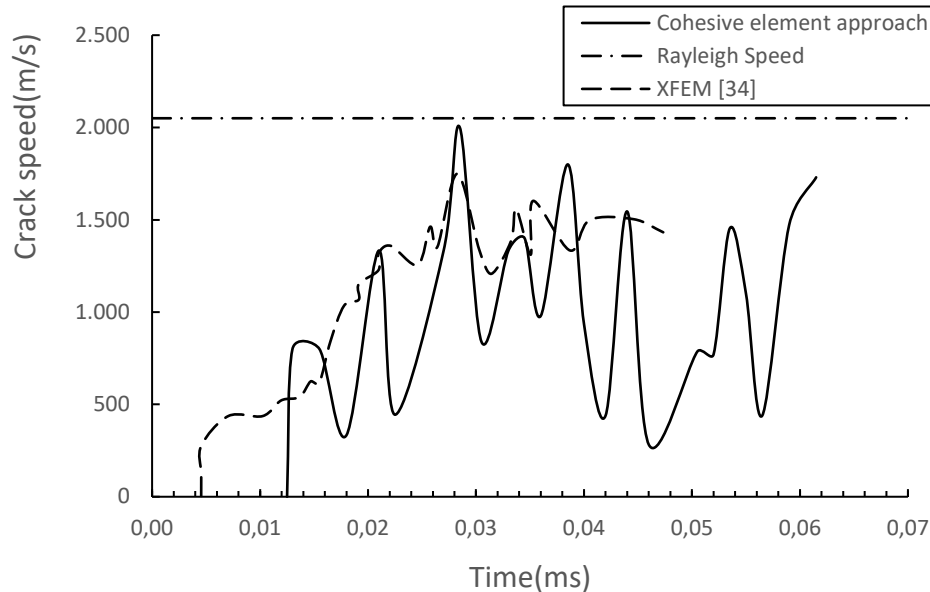


Figure 20. Crack propagation speed

6. Conclusion

A comprehensive study about cohesive elements and artificial compliance is carried out in this paper. It is concluded that by choosing the proper cohesive stiffness and element size, the effect of artificial compliance can be negligible without increasing the computational cost too much. A comparison between bilinear and exponential cohesive law is also carried out. From the initial stiffness and cyclic loading point of view, bilinear cohesive law is superior to exponential cohesive law if cohesive elements are used between every element interfaces. Cohesive zone enlargement approach is adopted in arbitrary crack propagation, and it is modified to apply only to the region near crack tip. Benchmark studies of Kalthoff experiment and dynamic crack branching test are used to prove the feasibility of modified cohesive zone enlargement approach. These results verify that using cohesive zone enlargement approach allows us to use relatively large mesh size, and capture the crack shape and crack speed at the same time.

References

- [1] Dugdale D. Yielding of steel sheets containing slits. *J Mech Phys Solids* 1960;8:100-4.
- [2] Barenblatt GI. The mathematical theory of equilibrium cracks in brittle fracture. *Adv Appl Mech* 1962;7:55-129.
- [3] Camanho PP, Dávila CG. Mixed-mode decohesion finite elements for the simulation of delamination in composite materials. 2002.
- [4] Pinho ST, Iannucci L, Robinson P. Formulation and implementation of decohesion elements in an explicit finite element code. *Composites Part A: Applied Science and Manufacturing* 2006;37:778-89.
- [5] Turon A, Davila CG, Camanho PP, Costa J. An engineering solution for mesh size effects in the simulation of delamination using cohesive zone models. *Eng Fract Mech* 2007;74:1665-82.
- [6] Hillerborg A, Modéer M, Petersson P. Analysis of crack formation and crack growth in concrete by means of fracture mechanics and finite elements. *Cem Concr Res* 1976;6:773-81.
- [7] Song SH, Paulino GH, Buttlar WG. Simulation of crack propagation in asphalt concrete using an intrinsic cohesive zone model. *J Eng Mech* 2006;132:1215-23.
- [8] Blackman B, Hadavinia H, Kinloch A, Williams J. The use of a cohesive zone model to study the fracture of fibre composites and adhesively-bonded joints. *Int J Fract* 2003;119:25-46.
- [9] Xu X, Needleman A. Numerical simulations of fast crack growth in brittle solids. *J Mech Phys Solids* 1994;42:1397-434.
- [10] Falk ML, Needleman A, Rice JR. A critical evaluation of cohesive zone models of dynamic fracture. *Le Journal de Physique IV* 2001;11:Pr5,43-Pr5-50.
- [11] Klein P, Foulk J, Chen E, Wimmer S, Gao H. Physics-based modeling of brittle fracture: cohesive formulations and the application of meshfree methods. *Theor Appl Fract Mech* 2001;37:99-166.
- [12] Espinosa HD, Zavattieri PD. A grain level model for the study of failure initiation and evolution in polycrystalline brittle materials. Part I: Theory and numerical implementation. *Mech Mater* 2003;35:333-64.
- [13] Murphy N, Ivankovic A. The prediction of dynamic fracture evolution in PMMA using a cohesive zone model. *Eng Fract Mech* 2005;72:861-75.
- [14] Camacho GT, Ortiz M. Computational modelling of impact damage in brittle materials. *Int J Solids Structures* 1996;33:2899-938.
- [15] Dooley I, Mangala S, Kale L, Geubelle P. Parallel simulations of dynamic fracture using extrinsic cohesive elements. *J Sci Comput* 2009;39:144-65.
- [16] Radovitzky R, Seagraves A, Tupek M, Noels L. A scalable 3D fracture and fragmentation algorithm based on a hybrid, discontinuous Galerkin, cohesive element method. *Comput Methods Appl Mech Eng* 2011;200:326-44.
- [17] Nguyen VP. An open source program to generate zero-thickness cohesive interface elements. *Adv Eng Software* 2014;74:27-39.
- [18] Blal N, Daridon L, Monerie Y, Pagano S. Artificial compliance inherent to the intrinsic cohesive zone models: criteria and application to planar meshes. *Int J Fract* 2012;178:71-83.
- [19] Blal N, Daridon L, Monerie Y, Pagano S. Micromechanical-based criteria for the calibration of cohesive zone parameters. *J Comput Appl Math* 2013;246:206-14.
- [20] Tomar V, Zhai J, Zhou M. Bounds for element size in a variable stiffness cohesive finite element model. *Int J Numer Methods Eng* 2004;61:1894-920.
- [21] Harper PW, Hallett SR. Cohesive zone length in numerical simulations of composite delamination. *Eng Fract Mech* 2008;75:4774-92.
- [22] Turon A, Camanho PP, Costa J, Dávila C. A damage model for the simulation of delamination in advanced composites under variable-mode loading. *Mech Mater* 2006;38:1072-89.
- [23] Shabir Z, Van der Giessen E, Duarte C, Simone A. The role of cohesive properties on intergranular crack propagation in brittle polycrystals. *Modell Simul Mater Sci Eng* 2011;19:035006.
- [24] Klein P, Foulk J, Chen E, Wimmer S, Gao H. Physics-based modeling of brittle fracture: cohesive formulations and the application of meshfree methods. *Theor Appl Fract Mech* 2001;37:99-166.
- [25] Klein P, Foulk J, Chen E, Wimmer S, Gao H. Physics-based modeling of brittle fracture: cohesive formulations and the application of meshfree methods. *Theor Appl Fract Mech* 2001;37:99-166.
- [26] Nakamura T, Wang Z. Simulations of crack propagation in porous materials. *Journal of applied mechanics* 2001;68:242-51.
- [27] Belytschil T, Chen H, Xu J, Zi G. Dynamic crack propagation based on loss of hyperbolicity and a new discontinuous enrichment. *Int J.Numer.Mel/i.Eng/it* 2003;58:1873-1905.
- [28] Van den Bosch M, Schreurs P, Geers M. An improved description of the exponential Xu and Needleman cohesive zone law for mixed-mode decohesion. *Eng Fract Mech* 2006;73:1220-34.
- [29] Tijssens MG, Sluys BL, van der Giessen E. Numerical simulation of quasi-brittle fracture using damaging cohesive surfaces. *European Journal of Mechanics-A/Solids* 2000;19:761-79.
- [30] Song J, Wang H, Belytschko T. A comparative study on finite element methods for dynamic fracture. *Comput Mech* 2008;42:239-50.
- [31] Ritchie RO, Francis B, Server WL. Evaluation of toughness in AISI 4340 alloy steel austenitized at low and high temperatures. *Metallurgical and Materials Transactions A* 1976;7:831-8.

- [32] Hong S, Kim H, Huh D, Suryanarayana C, Chun BS. Effect of clustering on the mechanical properties of SiC particulate-reinforced aluminum alloy 2024 metal matrix composites. *Materials Science and Engineering: A* 2003;347:198-204.
- [33] Turon A, Davila CG, Camanho PP, Costa J. An engineering solution for mesh size effects in the simulation of delamination using cohesive zone models. *Eng Fract Mech* 2007;74:1665-82.
- [34] Hillerborg A, Mod er M, Petersson P. Analysis of crack formation and crack growth in concrete by means of fracture mechanics and finite elements. *Cem Concr Res* 1976;6:773-81.
- [35] Palmer AC, Rice J. The growth of slip surfaces in the progressive failure of over-consolidated clay. 1973;332:527-48.
- [36] Menouillard T, Rethore J, Combescure A, Bung H. Efficient explicit time stepping for the eXtended Finite Element Method (X-FEM). *Int J Numer Methods Eng* 2006;68:911-39.
- [37] Rabczuk T, Zi G, Bordas S, Nguyen-Xuan H. A simple and robust three-dimensional cracking-particle method without enrichment. *Comput Methods Appl Mech Eng* 2010;199:2437-55.
- [38] Belytschko T, Chen H, Xu J, Zi G. Dynamic crack propagation based on loss of hyperbolicity and a new discontinuous enrichment. *Int J Numer Methods Eng* 2003;58:1873-905.
- [39] Ha YD, Bobaru F. Studies of dynamic crack propagation and crack branching with peridynamics. *Int J Fract* 2010;162:229-44.